photonics

MDPI

Article

Unveiling the Internal Dynamics of Rectangular Pulses in an Ultrafast Fiber Laser with MoS_2 Saturable Absorber

Jiangbo Feng [1,*], Yun Chen [1], Ming Li [2], Jiayi Zhang [3], Yanqian Lu [3], Huaquan Su [3] and Zhenhong Wang [4,*]

[1] Electric Power Research Institute of Guangdong Power Grid Co., Ltd., Guangzhou 510006, China
[2] Maoming Power Supply Bureau, Guangdong Power Grid Co., Ltd., Maoming 524500, China
[3] Digital and Intelligent Operations Center, Guangdong Power Grid Co., Ltd., Guangzhou 510180, China
[4] College of Electronics and Information Engineering, Shenzhen University, Shenzhen 518060, China
* Correspondence: fengjiangbo1995@163.com (J.F.); wangzhenhong@szu.edu.cn (Z.W.)

Abstract

In this work, we demonstrate the generation and evolution behaviors of rectangular pulses in a passively mode-locked erbium-doped fiber laser incorporating a molybdenum disulfide (MoS_2) saturable absorber. At lower pump power, the laser operates in a stable fundamental mode-locked state. With the gradual increase in pump power and appropriate polarization adjustment, the rectangular-pulse regime with spectral sidebands emerges, and the corresponding temporal width broadens from 0.34 ns to 0.85 ns as the pump increases. The dispersive Fourier transform measurements are employed to capture the real-time spectral evolution of the generated rectangular pulses, revealing that such pulses consist of chaotic sub-pulses with randomly varying intensities. Furthermore, the numerical simulations are in reasonable agreement with the experimental observations. Our results shed light on the pulse dynamics governing the transition and temporal width broadening, contributing to a deeper understanding of the underlying nonlinear phenomena in ultrafast fiber lasers.

Keywords: fiber laser; saturable absorber; rectangular pulses; real-time dynamics; numerical simulation

1. Introduction

Passively mode-locked fiber lasers are widely investigated as compact ultrafast sources because of their high beam quality, flexible cavity design, and compatibility with all-fiber integration [1,2]. Pulse formation in these lasers is governed by the combined action of dispersion, Kerr nonlinearity, gain, loss, and saturable absorption. Depending on the cavity parameters, conventional solitons, dispersion-managed solitons, dissipative solitons, noise-like pulses, and harmonic mode-locking states can be supported [2–5]. This diversity makes mode-locked fiber lasers useful platforms for studying nonlinear pulse evolution in dissipative systems [1–3]. The initiation and stability of passive mode locking depend fundamentally on the nonlinear response of saturable absorbers [6–8]. Among various nanomaterials, molybdenum disulfide (MoS_2) has matured into a standard platform for fiber lasers due to its reliable broadband absorption and compatibility with fiber systems [9,10]. Extensive research has already demonstrated its versatility in supporting diverse pulse regimes, ranging from conventional solitons to high-energy rectangular pulses [11–14]. However, while these pulse states are well documented, the underlying correlation between pump-dependent envelope broadening and round-trip-resolved internal dynamics remains insufficiently explored.

Check for updates

Received: 29 July 2026
Revised: 25 August 2026
Accepted: 2 September 2026
Published: 7 September 2026

Copyright: © 2026 by the authors. Licensee MDPI, Basel, Switzerland. This article is an open access article distributed under the terms and conditions of the Creative Commons Attribution (CC BY) license.

Rectangular temporal envelopes can occur in several mode-locking regimes and therefore cannot be classified from the averaged pulse shape alone. In dissipative soliton resonance (DSR), the pulse duration increases with pump power while the peak power remains nearly clamped, allowing the pulse energy to scale mainly through temporal broadening [15,16]. Wu et al. experimentally observed DSR in an all-normal-dispersion erbium-doped fiber laser [17], whereas Duan et al. demonstrated similar pulse-duration growth in the anomalous-dispersion regime [18]. Subsequent studies reported wide duration tuning [19,20], vector DSR and pulse compression [21,22], switchable DSR and rectangular noise-like pulses [23], period-doubling evolution [24], and the corresponding formation mechanism [25]. By contrast, a rectangular noise-like pulse is a long wave packet containing rapidly fluctuating ultrashort sub-pulses. Although rectangular pulses have been extensively studied, a unified understanding of how their pump-driven envelope broadening is linked to the round-trip-resolved evolution of the constituent sub-pulses is still lacking. Previous studies have established several important characteristics of rectangular pulses, but their primary objectives differ from those of the present work. Ref. [13] mainly focused on high-power and large-energy rectangular-pulse generation using a high-damage-threshold MoS_2 saturable absorber. Ref. [26] investigated the coexistence and pump-dependent evolution of rectangular and Gaussian-shaped noise-like pulses in a figure-eight fiber laser and qualitatively attributed the broadening of the rectangular pulse to the generation of additional internal sub-pulses. However, in these studies, the internal evolution responsible for the macroscopic envelope broadening was mainly inferred from averaged pulse characteristics. A direct connection between the pump-dependent envelope evolution and the nonrepeating round-trip dynamics remained insufficiently resolved.

Compared with the topological-insulator-based dual-wavelength rectangular-pulse laser reported in Ref. [27], which generated 13.62–25.16 ns pulses at a repetition rate of 3.54 MHz and mainly emphasized dual-wavelength operation, dispersion-dependent pulse shaping, and harmonic mode locking, the present MoS_2-assisted laser employs a laser cavity of approximately 20.2 m and produces sub-nanosecond rectangular wave packets with widths of 0.34–0.85 ns at a repetition rate of 9.88 MHz. More broadly, two-dimensional materials provide compact passive mode-locking platforms with rich nonlinear optical responses [28]. Within this material landscape, the main advantage of the present laser is not a higher output pulse energy but the combination of a compact fiber-compatible architecture with round-trip-resolved dispersive Fourier transform (DFT) measurements, quantitative fluctuation statistics, and numerical modeling, which enables pump-dependent envelope broadening to be linked directly to the stochastic redistribution and temporal expansion of the internal sub-pulse ensemble.

In this work, we investigate the generation and pump-dependent evolution of rectangular pulses in a passively mode-locked erbium-doped fiber laser incorporating an MoS_2 saturable absorber. At low pump power, the laser operates in a stable fundamental mode-locked state. At higher pump levels and under an appropriately adjusted intracavity polarization state, rectangular pulses with modulated spectral wings are obtained. Once the rectangular-pulse regime is established, the measured envelope width increases from 0.34 ns to 0.85 ns as the pump power is raised from 350 mW to 502 mW. Round-trip-resolved DFT measurements reveal nonrepeating spectral-intensity fluctuations within the rectangular wave packet, while the numerical simulations show that increasing the available gain energy expands the temporal region occupied by the internal sub-pulses. By combining these observations, the present work goes beyond the generation and averaged characterization of rectangular pulses and provides an experiment–simulation-supported connection between the macroscopic envelope broadening and the evolution of the internal stochastic sub-pulse ensemble.

2. Experimental Setup

Figure 1a depicts the ring-cavity configuration employed in the experiment. Optical gain is provided by a 2.5 m erbium-doped fiber (EDF) with a core absorption of 14.2 dB/m at 980 nm. Pump radiation from a 980 nm laser diode is introduced into the cavity through a 980/1550 nm wavelength-division multiplexer (WDM). Passive mode locking is initiated by a microfiber-based MoS_2 saturable absorber prepared according to the method reported in Ref. [29]. A polarization controller (PC, Thorlabs, New Jersey, NJ, USA) is used to tune the intracavity polarization, whereas a polarization-independent isolator (PI-ISO) fixes the propagation direction. The cavity also contains approximately 10 m of standard single-mode fiber (SMF), and 20% of the circulating optical power is extracted through the 20% arm of a 20/80 optical coupler. The resulting cavity length is approximately 20.2 m. Using dispersion coefficients of 21.7 ps^2/km for the EDF and −23 ps^2/km for the SMF at 1550 nm, the net cavity dispersion is estimated to be approximately −0.35 ps^2 [30]. Optical spectra are acquired with an AQ6370D optical spectrum analyzer (Yokogawa, Tokyo, Japan). Temporal pulse trains and RF spectra are recorded using a 4-GHz RTP044 oscilloscope (Rohde & Schwarz, Munich, Germany) and a SSA5023A RF spectrum analyzer (Siglent, Shenzhen, China), respectively, while pulse-width characterization is performed with a FR103HS autocorrelator (Femtochrome, Berkeley, CA, USA).

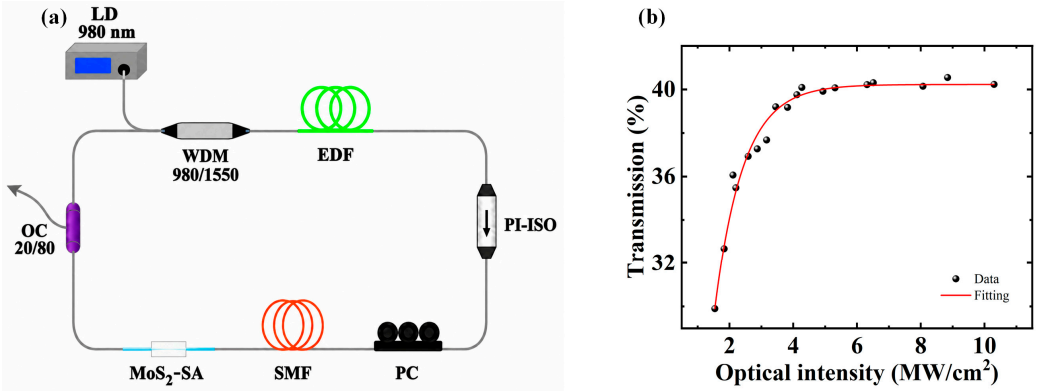


Figure 1. (**a**) Schematic of the passively mode-locked fiber laser. LD, laser diode; WDM, wavelength-division multiplexer; EDF, erbium-doped fiber; PI-ISO, polarization-independent isolator; PC, polarization controller; SMF, single-mode fiber; MoS_2-SA, molybdenum disulfide saturable absorber; OC, optical coupler. (**b**) Saturable absorption characteristics of MoS_2 and the corresponding fitting curve.

The saturable absorption characteristics of MoS_2 are shown in Figure 1b. The transmission increases with incident optical intensity and gradually approaches a saturated plateau. The modulation depth and non-saturable loss are about 39% and approximately 59.8%, respectively, and the saturation intensity is estimated to be ~4 MW/cm^2.

3. Results and Discussion

With the pump fixed at 22 mW, the laser reaches a stable fundamental mode-locked state, whose output characteristics are presented in Figure 2. The optical spectrum in Figure 2a is centered at 1559.1 nm and spans 5 nm at the 3 dB level, with several sidebands appearing around the main spectral envelope. The slight spectral tilt and unequal sideband intensities are mainly attributed to residual intracavity birefringence. The single-mode fiber supports two orthogonal polarization eigenmodes. These wavelength-dependent phase delays, together with weak polarization-dependent loss in practical cavity components, produce an effective wavelength-dependent transmission that favors one spectral side. The nonuniform EDF gain profile and residual higher-order dispersion may further contribute to the overall tilt and slight sideband imbalance [31,32]. Figure 2b displays a uniform pulse

train with a temporal separation of 101.2 ns, corresponding to the cavity repetition rate of approximately 9.88 MHz. At a pump power of 22 mW, the measured average output power is approximately 0.2 mW, corresponding to the pulse energy of ~0.02 nJ. The RF spectrum in Figure 2c shows a distinct fundamental component at the same frequency, exceeding the background by more than 60 dB and thereby confirming the stability of the mode-locked operation. As shown in Figure 2d, the fitted autocorrelation trace has an FWHM of approximately 1.8 ps. After deconvolution based on a sech^2 pulse profile, the pulse duration is estimated to be about 1.1 ps. The corresponding dimensionless time–bandwidth product is approximately 0.72, indicating that the pulses are chirped. This low-pump state serves as the reference for analyzing the subsequent formation and evolution of the rectangular pulses.

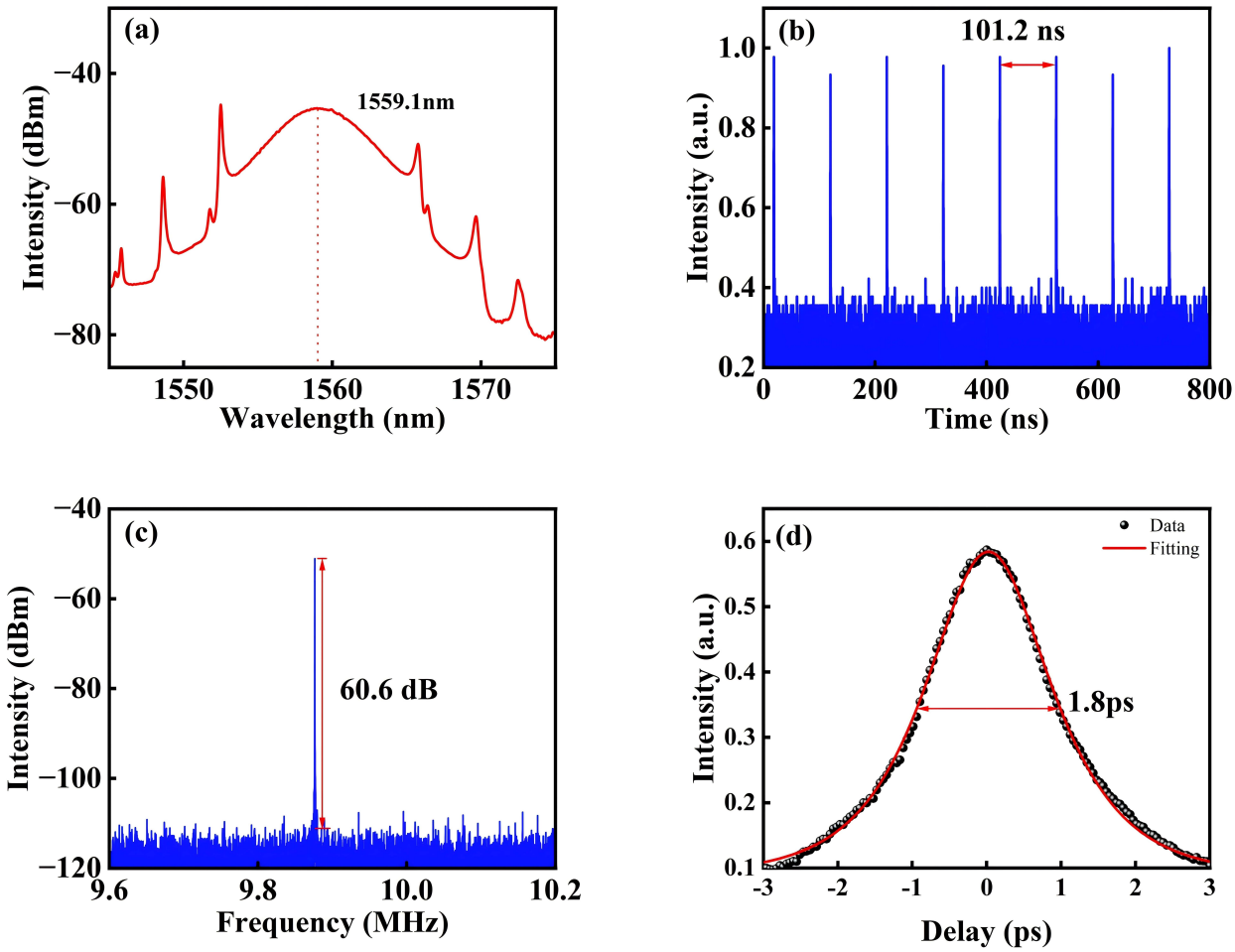


Figure 2. Characteristics of the fundamental mode-locked state at a pump power of 22 mW: (**a**) optical spectrum; (**b**) temporal pulse train; (**c**) RF spectrum; (**d**) autocorrelation trace.

At a pump power of 250 mW, the laser exhibits the transition state shown in Figure 3. The optical spectrum in Figure 3a is centered at 1558.9 nm with a 3 dB bandwidth of 3.7 nm. The optical spectrum has broadened and displays clear sidebands around the central envelope, while the temporal trace retains a regular pulse train with the 101.2 ns cavity period but does not yet show a clearly resolved rectangular envelope (Figure 3b). The fundamental RF peak remains distinct, with an SNR of 58.7 dB (Figure 3c), and the fitted autocorrelation trace has an FWHM of approximately 1.2 ps (Figure 3d). Assuming a sech^2 pulse profile, the pulse duration is estimated to be approximately 0.78 ps. From the above, the TBP at a pump power of 250 mW is approximately 0.36. These characteristics identify

an intermediate state between the fundamental mode-locked output and the established rectangular-pulse regime.

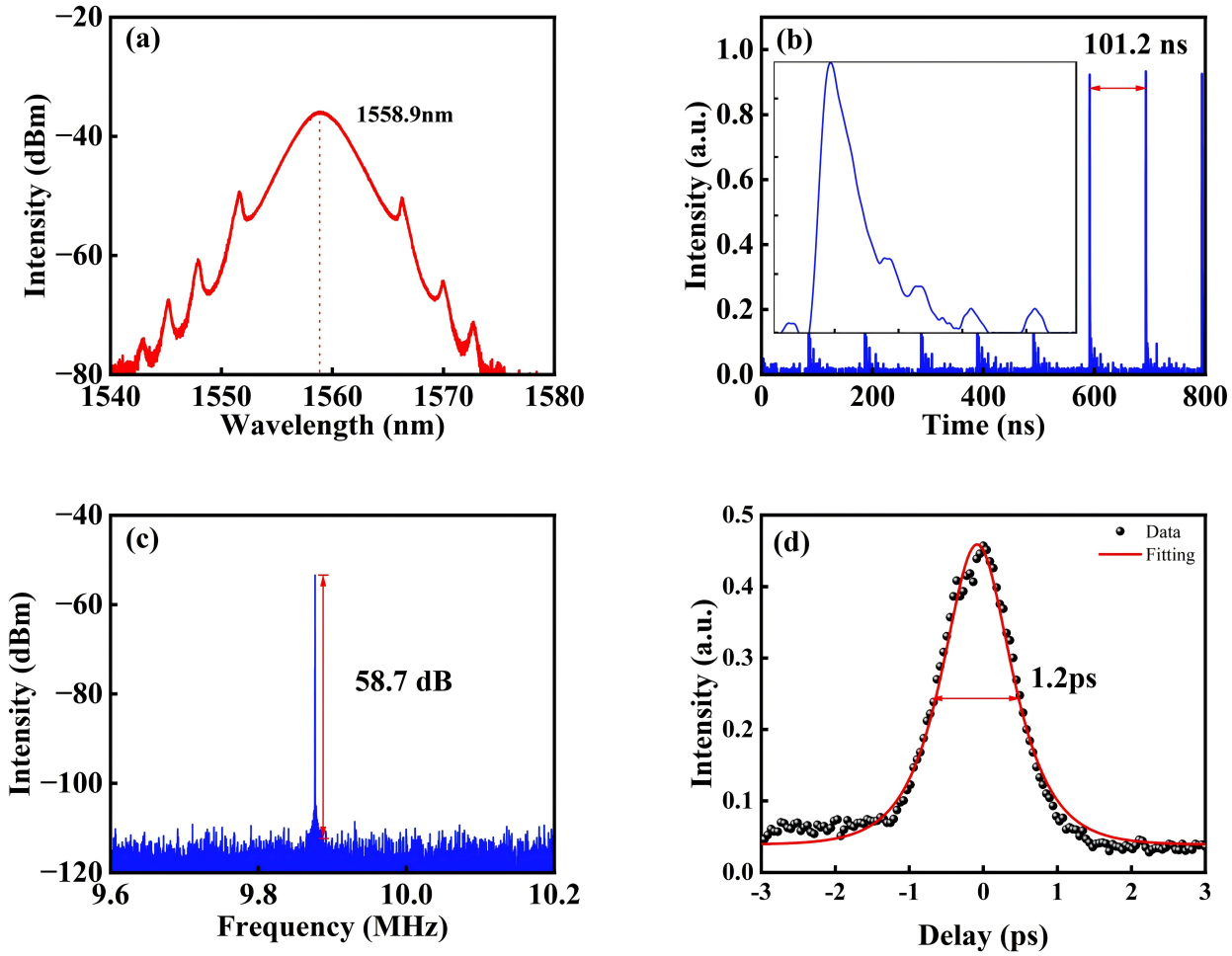


Figure 3. Characteristics of the transition state at a pump power of 250 mW: (**a**) optical spectrum; (**b**) temporal pulse train; (**c**) RF spectrum; (**d**) autocorrelation trace and fit.

Starting from the 250 mW transition state, the PC is kept fixed while the pump power is increased to 350 mW. Under these conditions, a clearly defined rectangular pulse emerged, as shown in Figure 4. Compared with Figure 2a, the optical spectrum in Figure 4a expands to approximately 1540–1578 nm and forms a broad envelope centered at 1558.3 nm, with several local sidebands or modulated features on the spectral wings. The pulse train in Figure 4b retains the 101.2 ns cavity period, whereas the enlarged single-pulse trace shows a rectangular envelope with an FWHM of 0.34 ns. The fundamental RF peak remains distinct and has an SNR of 60.2 dB (Figure 4c). Figure 4d shows a narrow autocorrelation feature with a fitted FWHM of approximately 1.12 ps. The corresponding time–bandwidth product is determined to be approximately 1.09. This coexistence of nanosecond and picosecond scales is consistent with reported noise-like and rectangular noise-like pulses containing ultrashort sub-pulses within a longer envelope [26,33–35].

Furthermore, to resolve the internal evolution over consecutive cavity round trips, DFT measurements are employed [36]. Figure 5 presents the three-dimensional shot-to-shot spectral evolution over 1000 round trips at pump powers of 250, 350, and 450 mW. At 250 mW (Figure 5a), corresponding to the transition state, the spectra are concentrated around 1560 nm, while the positions and amplitudes of the local spectral maxima vary continuously from round trip to round trip. At 350 mW (Figure 5b), a well-defined rectangular

envelope with an FWHM of 0.34 ns is established, and the single-shot spectra exhibit a broad distribution with pronounced nonrepeating fluctuations. When the pump power is further increased to 450 mW (Figure 5c), the rectangular envelope broadens to 0.70 ns, whereas the broad spectral distribution and irregular round-trip-to-round-trip variations persist. The 250 mW result characterizes the internal fluctuations of the transition state, whereas the comparison between 350 and 450 mW directly addresses pump-dependent broadening within the established rectangular-pulse regime. This comparison shows that the temporal envelope broadening is accompanied by persistent stochastic rearrangement of the internal sub-pulse ensemble, rather than convergence toward a stationary single-pulse state. Together with the picosecond autocorrelation feature, these observations support the interpretation that the rectangular wave packet consists of numerous noise-like sub-pulses with randomly varying intensities [26,33–35,37].

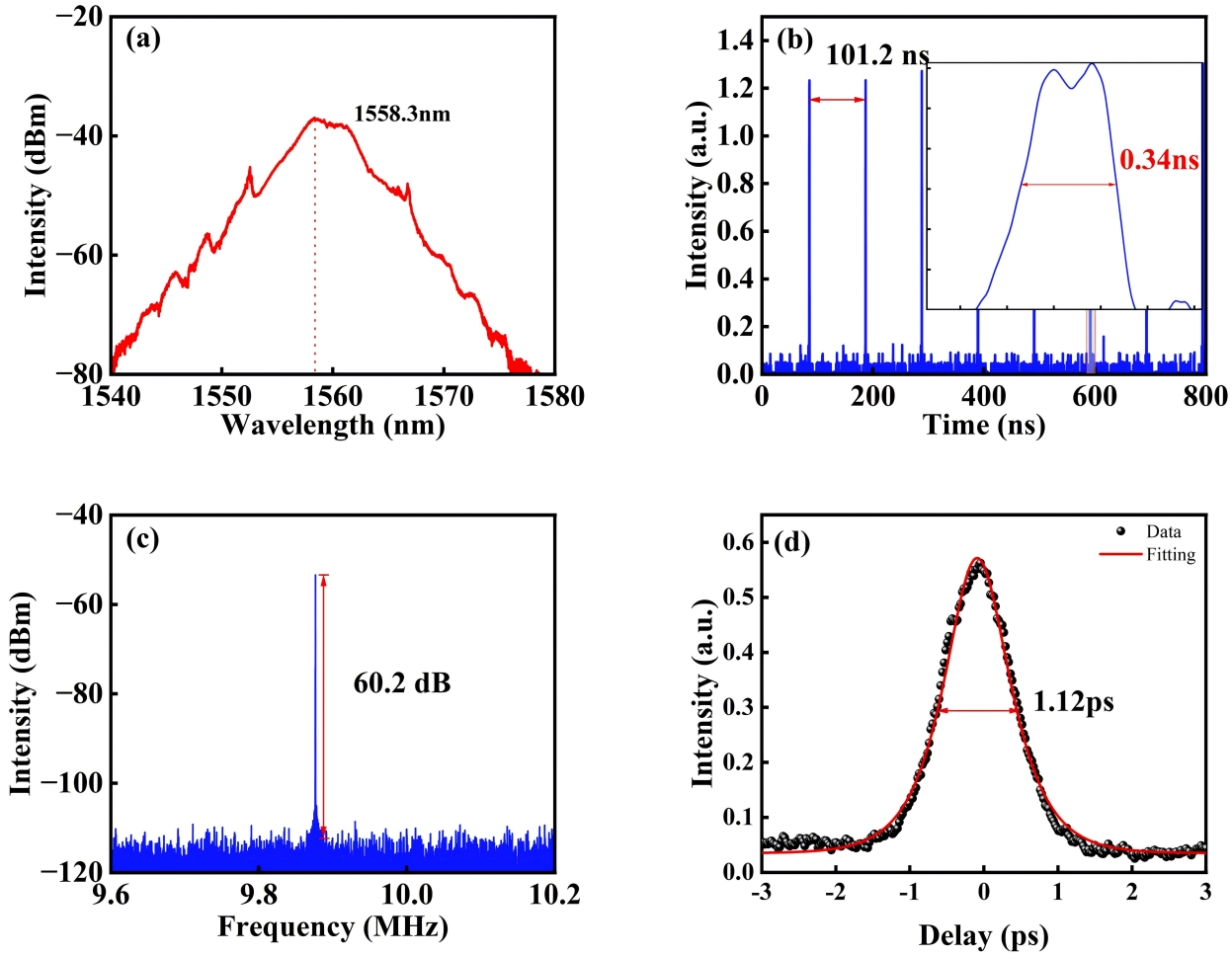


Figure 4. Characteristics of the rectangular-pulse state at a pump power of 350 mW: (**a**) optical spectrum; (**b**) temporal pulse train, with an enlarged rectangular envelope in the inset; (**c**) RF spectrum; (**d**) autocorrelation trace and fit.

To quantify the shot-to-shot fluctuations shown in Figure 5, the relative spectral energy of each round trip is obtained by integrating the DFT spectrum over the same signal window. The normalized values are plotted as the white traces in Figure 5. The relative standard deviations are 1.30%, 1.47%, and 0.84% at pump powers of 250, 350, and 450 mW, respectively. The wavelength-resolved coefficient of variation is further evaluated to characterize the spectral-intensity fluctuations across the measured wavelength range. To reduce the influence of background noise, the average value is evaluated only over the spectral region where the ensemble-averaged intensity exceeded 10% of its maximum. The

resulting average coefficients of variation are 17.7%, 18.8%, and 13.5% at 250, 350, and 450 mW, respectively. These values are much larger than the fluctuations in the integrated spectral energy, indicating that the total spectral energy remains relatively stable while the internal spectral distribution varies noticeably from one round trip to the next. The 250 mW result corresponds to the transition state. At 350 and 450 mW, the coefficients of variation remain 18.8% and 13.5%, respectively, showing that stochastic internal spectral fluctuations persist after the rectangular-pulse regime is established. The fluctuation level does not show a monotonic dependence on pump power.

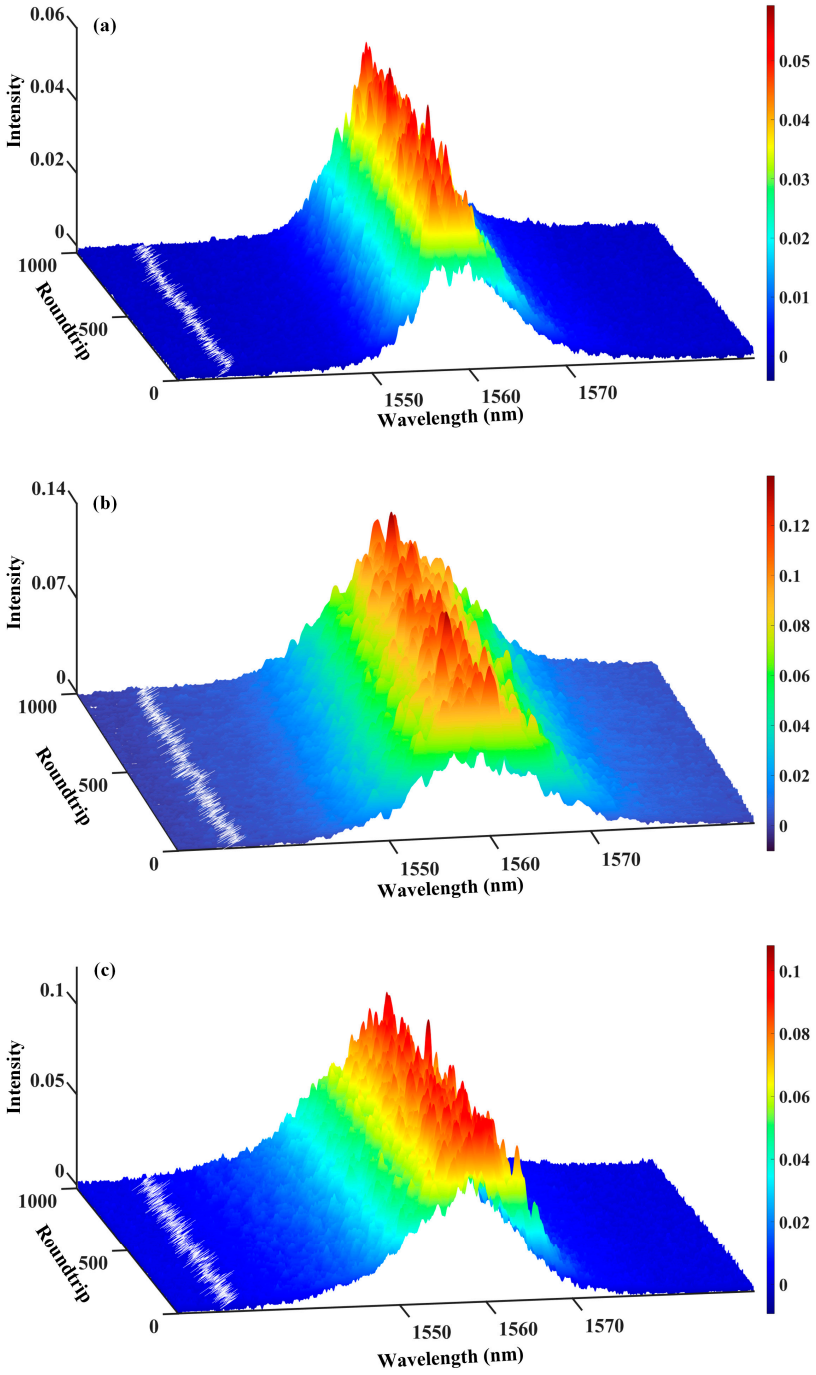


Figure 5. Three-dimensional shot-to-shot spectral evolution over 1000 round trips at pump powers of (**a**) 250 mW, (**b**) 350 mW, and (**c**) 450 mW. The white traces represent the normalized relative spectral energy, obtained by integrating each background-corrected DFT spectrum over the same signal window.

In addition, Figure 6 summarizes the pump-dependent temporal and energy evolution across the rectangular-pulse regime. The temporal profiles in Figure 6a show systematic broadening: the rectangular-envelope FWHM increases from 0.34 ns at 350 mW to 0.43 ns at 400 mW, 0.70 ns at 450 mW, and 0.85 ns at 502 mW. The largest measured increment occurs between 400 and 450 mW. No pulse splitting is visible in the displayed temporal traces, and the overall rectangular shape is maintained throughout the measured sequence. Pump-dependent temporal expansion without pulse breakup has also been reported for rectangular noise-like pulse regimes in other fiber-laser configurations [33,35,38,39]. As shown in Figure 6b, the average output power increases approximately linearly from about 3.1 mW at a pump power of 250 mW to about 6.1 mW at 502 mW. Because the repetition rate remains approximately 9.88 MHz, the calculated average pulse energy increases from approximately 0.31 nJ to 0.62 nJ. Within the rectangular-pulse regime, the simultaneous increases in average pulse energy and temporal FWHM show that the additional pulse energy is accompanied by expansion of the rectangular wave packet, consistent with the energy-scaling behavior reported for rectangular noise-like pulses [38,39].

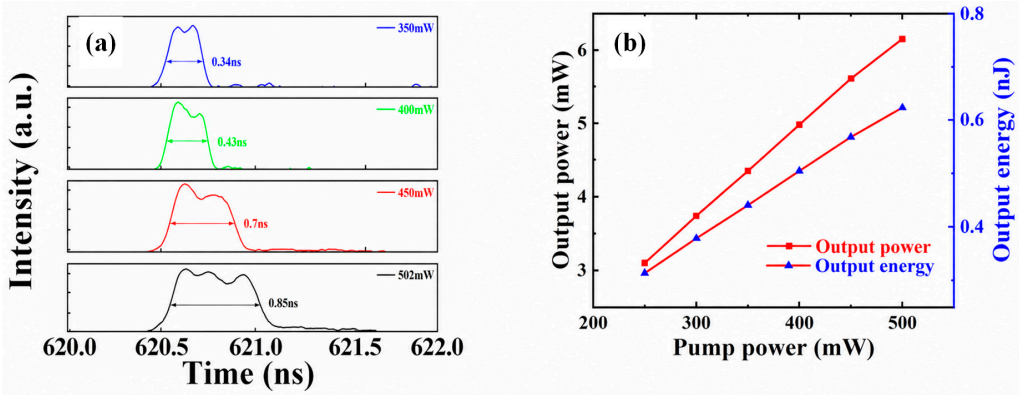


Figure 6. Pump-power-dependent output characteristics: (**a**) rectangular temporal profiles at 350, 400, 450, and 502 mW; (**b**) average output power and pulse energy as functions of pump power.

Overall, the experimental measurements establish an evolution from stable fundamental mode locking to a rectangular-pulse state under increased pump power and appropriate polarization adjustment. Once the rectangular regime is obtained, the envelope FWHM increases monotonically from 0.34 ns to 0.85 ns as the pump power rises from 350 mW to 502 mW, while the fundamental repetition rate and high RF SNR are maintained. The DFT record at 250 mW characterizes the shot-to-shot spectral fluctuations of the transition state. At 350 and 450 mW, the wavelength-resolved spectral-intensity coefficients of variation remain 18.8% and 13.5%, respectively, confirming that stochastic internal spectral fluctuations persist after the rectangular-pulse regime is established. Combining these quantitative statistics with the pump-dependent temporal measurements provides a direct connection between envelope broadening and internal spectral dynamics. As the rectangular-envelope FWHM increases from 0.34 ns at 350 mW to 0.70 ns at 450 mW, a spectral-intensity coefficient of variation of 13.5% remains at 450 mW. This correspondence demonstrates that pump-induced envelope broadening does not eliminate the stochastic internal spectral dynamics of the rectangular wave packet, although the fluctuation magnitude does not increase monotonically with pump power.

4. Numerical Simulation

Numerical simulations of the laser operation are conducted to qualitatively reproduce the experimentally observed broadening and internal evolution of the rectangular wave

packet as the available gain energy increases [40]. The numerical model is established using the complex Ginzburg–Landau equation [41]:

$$\frac{\partial Y}{\partial z} = -i\frac{\beta_2}{2}\frac{\partial^2 Y}{\partial T^2} + i\gamma|Y|^2 Y + \frac{g-\alpha}{2}Y + \frac{g}{2\Omega_g^2}\frac{\partial^2 Y}{\partial T^2} \quad (1)$$

where Y is the slowly varying field envelope, z denotes the propagation distance, and T is the retarded time. The parameters β_2, γ, and α denote the second-order dispersion, nonlinear coefficient, and intracavity loss, respectively, whereas g and Ω_g describe the saturated gain and EDF gain bandwidth. The gain g is defined by the following expression:

$$g = g_0\frac{E_s}{E_s + \int(|Y|^2)dT} \quad (2)$$

Here, g_0 denotes the small-signal gain coefficient, and E_s represents the effective gain-saturation energy. In an erbium-doped fiber, both parameters are related to the pump level, although they describe different aspects of the gain process. A higher pump power increases the population inversion and therefore raises the available gain. It also increases the energy that can be stored and replenished in the gain medium. In the present lumped model, this latter effect is represented by E_s.

The model is used here to reproduce the qualitative energy-scaling behavior observed experimentally, rather than to establish a direct calibration between pump power and the gain parameters. Following the reduced treatment commonly used in mode-locked fiber-laser simulations [22,40], g_0 is kept fixed and E_s is varied as the effective control parameter. For a given circulating pulse energy, a larger E_s weakens gain saturation and leaves more saturated gain available to the field. Keeping g_0 unchanged avoids varying two related gain parameters at the same time and makes it easier to identify the effect of gain saturation on the pulse evolution. Therefore, E_s = 0.4, 0.8, and 1.2 nJ are used to represent low, intermediate, and high effective gain-energy conditions, rather than specific experimental pump powers. A direct conversion between E_s and pump power would require a calibrated EDF rate-equation model that includes pump absorption, population inversion, spectroscopic parameters, and cavity losses.

A saturable absorber (SA) is employed as the passive mode-locking mechanism in the simulation. Because its recovery time is assumed to be much shorter than the pulse-evolution timescale, the SA is treated as instantaneous, and its response is described by the following simplified equation [42–44]:

$$T(t) = 1 - \alpha_{ns} - \frac{\alpha_n}{1 + |Y|^2/P_s} \quad (3)$$

In this equation, $T(t)$ is the intensity-dependent transmission, α_{ns} denotes the non-saturable loss, α_n represents the modulation depth, and P_s is the saturation power.

The numerical parameters are chosen close to the experimental cavity while retaining a tractable simulation window. The cavity contains 2.5 m of EDF and 17.7 m of SMF. For the EDF, β_2 = 21.7 ps^2/km and γ = 3 W^{-1}km^{-1}; for the SMF, β_2 = −23 ps^2/km and γ = 1.3 W^{-1}km^{-1}. These values yield a net cavity dispersion of approximately −0.36 ps^2. The small-signal gain is g_0 = 1100 km^{-1}, and the EDF gain bandwidth is 30 nm. The SA parameters are α_n = 0.39, α_{ns} = 0.598, and P_s = 100 W, and 20% of the intracavity power is extracted at the output coupler. With a total of 1000 cavity round trips simulated, all quantities are held constant except E_s, which is set to 0.4, 0.8, and 1.2 nJ.

Figure 7a–c compare the spectral build-up for the three gain-saturation energies. In every case, the intensity pattern changes from one round trip to the next and does not

exhibit a regular breathing period, indicating that the calculated state consists of an irregular ensemble of sub-pulses rather than a stationary single pulse. As E_s rises, the spectral traces become denser and their local contrast increases, whereas the overall bandwidth changes less markedly because the EDF gain bandwidth and the nonlinear dissipative balance continue to limit spectral expansion.

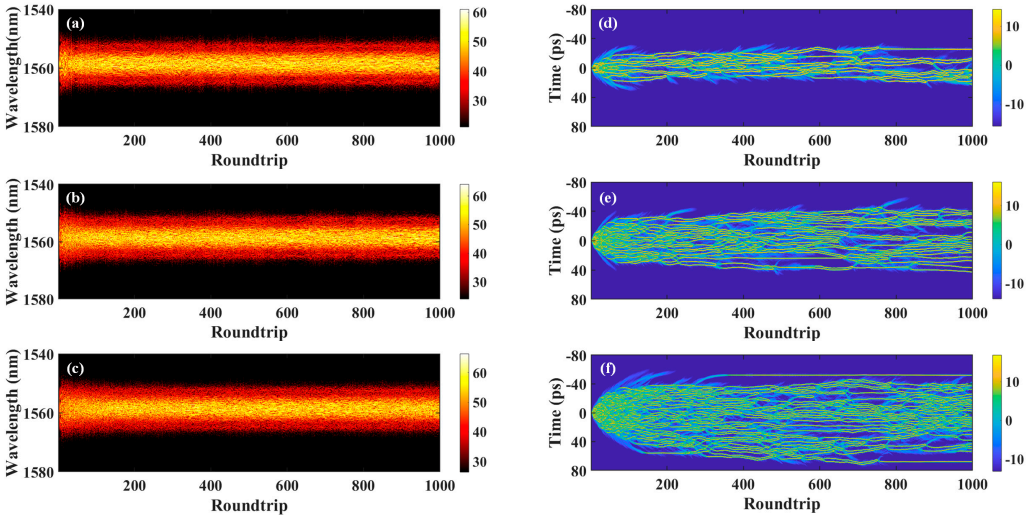


Figure 7. Effects of the gain-saturation energy on the pulse dynamics over 1000 cavity round trips: (**a**–**c**) spectral evolution and (**d**–**f**) temporal evolution for E_s = 0.4, 0.8, and 1.2 nJ, respectively.

The influence of E_s is most evident in the temporal maps shown in Figure 7d–f. At E_s = 0.4 nJ, most sub-pulse trajectories remain concentrated near the center of the temporal window. As E_s increases to 0.8 nJ, the occupied interval broadens and additional filament-like trajectories emerge. At E_s = 1.2 nJ, the pulse packet spans the widest temporal range and contains the largest number of distinguishable internal trajectories. This evolution indicates that the additional available energy is accommodated primarily through the generation and temporal spreading of sub-pulses rather than the unlimited growth of a single localized peak.

This behavior can be explained by the saturated-gain and SA responses described by Equations (2) and (3). For a given intracavity energy, a larger Es weakens gain saturation and allows more energy to accumulate, while the SA suppresses the weak background and favors intense localized structures. Meanwhile, dispersion and self-phase modulation continuously redistribute the energy within the pulse packet. Once a single pulse can no longer accommodate the available energy, pulse splitting and multi-pulsing become increasingly favorable [45]. Consequently, the progressive temporal expansion from Figure 7d–f agrees qualitatively with both the experimentally observed pump-dependent broadening of the rectangular envelope and the nonrepeating internal structures revealed by DFT measurements, confirming that increased available gain energy provides a viable route to enlarging the bounded, noise-like sub-pulse ensemble.

5. Conclusions

The MoS_2-assisted erbium-doped fiber laser exhibits a clear transition from fundamental mode locking to rectangular-pulse emission as the pump power and intracavity polarization state are adjusted. After the rectangular-pulse regime is established, increasing the pump power from 350 mW to 502 mW broadens the envelope FWHM from 0.34 ns to 0.85 ns, while the fundamental repetition rate remains approximately 9.88 MHz and a high RF signal-to-noise ratio is maintained. The nonrepeating round-trip spectra captured by DFT, together with the picosecond autocorrelation feature and pulse-energy fluctuations,

demonstrate the stochastic internal structure of the rectangular wave packet. Numerical simulations further show that the temporal region occupied by the internal sub-pulses expands as the available gain energy increases. This suggests that the additional gain energy is mainly accommodated by the formation and temporal spreading of more internal sub-pulses, rather than by continuous amplification of a single localized pulse. The resulting expansion of the internal sub-pulse ensemble is reflected in the broadening of the rectangular envelope observed experimentally. Compared with previous studies that mainly focused on high-energy pulse generation, pulse-shape coexistence, or averaged pump-dependent evolution, the present work links the measured envelope broadening with the round-trip-resolved internal dynamics through combined experimental observations and numerical simulations. Although the present results were obtained in an MoS_2-assisted fiber laser, the same interpretation may also be useful for understanding rectangular noise-like pulses in other dissipative fiber-laser systems with similar gain, saturable absorption, dispersion, and nonlinear effects.

Author Contributions: Conceptualization, J.F.; methodology, Y.C.; software, M.L.; validation, J.Z., Y.L.; formal analysis, H.S.; investigation, Y.C.; resources, M.L.; data curation, J.Z.; writing—original draft preparation, J.F.; writing—review and editing, Z.W.; visualization, Z.W.; supervision, Z.W. All authors have read and agreed to the published version of the manuscript.

Funding: No external grant funding was received for this study.

Data Availability Statement: The data supporting the findings of this study are not currently publicly available but can be obtained from the authors upon reasonable request.

Conflicts of Interest: Jiangbo Feng, Yun Chen, Ming Li, Jiayi Zhang, Yanqian Lu and Huaquan Su were employed by Guangdong Power Grid Co., Ltd. The remaining author declare that the research was conducted in the absence of any commercial or financial relationships that could be construed as a potential conflict of interest.

References

1. Fermann, M.E.; Hartl, I. Ultrafast Fibre Lasers. *Nat. Photonics* **2013**, *7*, 868–874. [CrossRef]
2. Song, Y.; Shi, X.; Wu, C.; Tang, D.; Zhang, H. Recent Progress of Study on Optical Solitons in Fiber Lasers. *Appl. Phys. Rev.* **2019**, *6*, 021313. [CrossRef]
3. Grelu, P.; Akhmediev, N. Dissipative Solitons for Mode-Locked Lasers. *Nat. Photonics* **2012**, *6*, 84–92. [CrossRef]
4. Renninger, W.H.; Chong, A.; Wise, F.W. Dissipative Solitons in Normal-Dispersion Fiber Lasers. *Phys. Rev. A* **2008**, *77*, 023814. [CrossRef]
5. Chong, A.; Buckley, J.; Renninger, W.; Wise, F. All-Normal-Dispersion Femtosecond Fiber Laser. *Opt. Express* **2006**, *14*, 10095–10100. [CrossRef] [PubMed]
6. Shang, X.; Xu, N.; Zong, M.; Guo, L.; Gao, G.; Zhang, Z.; Wang, Z.; Zhang, H.; Yu, W.; Li, L.; et al. Generation and Dynamics Behaviors of Various Soliton Phenomena in 1.5-μm Ultrafast Er-Doped Fiber Lasers. *J. Nonlinear Opt. Phys. Mater.* **2026**, 2650025. [CrossRef]
7. Shang, X.; Xu, N.; Zong, M.; Yu, W.; Guo, L.; Gao, G.; Zhang, Z.; Zhang, H.; Su, L. $ZrGeTe_4$ Nanoparticles as a Saturable Absorber for Mode-Locked Operations at 1 and 1.55 μm. *Photonics* **2026**, *13*, 305. [CrossRef]
8. Xu, N.; Zong, M.; Su, L.; Wang, Z.; Yu, W.; Fan, W.; Guo, L.; Fu, S.; Shang, X.; Zhang, H. Nonlinear Optical Properties of Tellurene Nanosheets for Harmonic Soliton Operations in an Er-Doped Fiber Laser. *Photonics* **2026**, *13*, 584. [CrossRef]
9. Zhang, H.; Lu, S.B.; Zheng, J.; Du, J.; Wen, S.C.; Tang, D.Y.; Loh, K.P. Molybdenum Disulfide (MoS_2) as a Broadband Saturable Absorber for Ultra-Fast Photonics. *Opt. Express* **2014**, *22*, 7249–7260. [CrossRef] [PubMed]
10. Woodward, R.I.; Howe, R.C.T.; Hu, G.; Torrisi, F.; Zhang, M.; Hasan, T.; Kelleher, E.J.R. Few-Layer MoS_2 Saturable Absorbers for Short-Pulse Laser Technology: Current Status and Future Perspectives [Invited]. *Photonics Res.* **2015**, *3*, A30–A42. [CrossRef]
11. Xia, H.; Li, H.; Lan, C.; Li, C.; Zhang, X.; Zhang, S.; Liu, Y. Ultrafast Erbium-Doped Fiber Laser Mode-Locked by a CVD-Grown Molybdenum Disulfide (MoS_2) Saturable Absorber. *Opt. Express* **2014**, *22*, 17341–17348. [CrossRef] [PubMed]
12. Khazaeizhad, R.; Kassani, S.H.; Jeong, H.; Yeom, D.-I.; Oh, K. Mode-Locking of Er-Doped Fiber Laser Using a Multilayer MoS2 Thin Film as a Saturable Absorber in Both Anomalous and Normal Dispersion Regimes. *Opt. Express* **2014**, *22*, 23732–23742. [CrossRef] [PubMed]

13. Ma, P.; Lin, W.; Zhang, H.; Xu, S.; Yang, Z. High-Power Large-Energy Rectangular Mode-Locked Er-Doped Fiber Laser Based on High-Damage-Threshold MoS_2 Saturable Absorber. *IEEE Photonics J.* **2019**, *11*, 1504312. [CrossRef]
14. Cui, Y.; Lu, F.; Liu, X. MoS_2-Clad Microfibre Laser Delivering Conventional, Dispersion-Managed and Dissipative Solitons. *Sci. Rep.* **2016**, *6*, 30524. [CrossRef] [PubMed]
15. Chang, W.; Ankiewicz, A.; Soto-Crespo, J.M.; Akhmediev, N. Dissipative Soliton Resonances. *Phys. Rev. A* **2008**, *78*, 023830. [CrossRef]
16. Chang, W.; Soto-Crespo, J.M.; Ankiewicz, A.; Akhmediev, N. Dissipative Soliton Resonances in the Anomalous Dispersion Regime. *Phys. Rev. A* **2009**, *79*, 033840. [CrossRef]
17. Wu, X.; Tang, D.Y.; Zhang, H.; Zhao, L.M. Dissipative Soliton Resonance in an All-Normal-Dispersion Erbium-Doped Fiber Laser. *Opt. Express* **2009**, *17*, 5580–5584. [CrossRef] [PubMed]
18. Duan, L.; Liu, X.; Mao, D.; Wang, L.; Wang, G. Experimental Observation of Dissipative Soliton Resonance in an Anomalous-Dispersion Fiber Laser. *Opt. Express* **2012**, *20*, 265–270. [CrossRef] [PubMed]
19. Luo, Z.-C.; Cao, W.-J.; Lin, Z.-B.; Cai, Z.-R.; Luo, A.-P.; Xu, W.-C. Pulse Dynamics of Dissipative Soliton Resonance with Large Duration-Tuning Range in a Fiber Ring Laser. *Opt. Lett.* **2012**, *37*, 4777–4779. [CrossRef] [PubMed]
20. Wang, S.-K.; Ning, Q.-Y.; Luo, A.-P.; Lin, Z.-B.; Luo, Z.-C.; Xu, W.-C. Dissipative Soliton Resonance in a Passively Mode-Locked Figure-Eight Fiber Laser. *Opt. Express* **2013**, *21*, 2402–2407. [CrossRef] [PubMed]
21. Luo, Z.-C.; Ning, Q.-Y.; Mo, H.-L.; Cui, H.; Liu, J.; Wu, L.-J.; Luo, A.-P.; Xu, W.-C. Vector Dissipative Soliton Resonance in a Fiber Laser. *Opt. Express* **2013**, *21*, 10199–10204. [CrossRef] [PubMed]
22. Li, D.; Li, L.; Zhou, J.; Zhao, L.; Tang, D.; Shen, D. Characterization and Compression of Dissipative-Soliton-Resonance Pulses in Fiber Lasers. *Sci. Rep.* **2016**, *6*, 23631. [CrossRef] [PubMed]
23. Deng, Z.-S.; Zhao, G.-K.; Yuan, J.-Q.; Lin, J.-P.; Chen, H.-J.; Liu, H.-Z.; Luo, A.-P.; Cui, H.; Luo, Z.-C.; Xu, W.-C. Switchable Generation of Rectangular Noise-like Pulse and Dissipative Soliton Resonance in a Fiber Laser. *Opt. Lett.* **2017**, *42*, 4517–4520. [CrossRef] [PubMed]
24. Wang, Y.; Su, L.; Wang, S.; Hua, L.; Li, L.; Shen, D.; Tang, D.; Komarov, A.; Klimczak, M.; Fu, S.; et al. Breach and Recurrence of Dissipative Soliton Resonance during Period-Doubling Evolution in a Fiber Laser. *Phys. Rev. A* **2020**, *102*, 013501. [CrossRef]
25. Li, D.; Tang, D.; Zhao, L.; Shen, D. Mechanism of Dissipative-Soliton-Resonance Generation in Passively Mode-Locked All-Normal-Dispersion Fiber Lasers. *J. Light. Technol.* **2015**, *33*, 3781–3787. [CrossRef]
26. Zhao, G.-K.; Chen, H.-J.; Liu, H.-Z.; Chen, W.-C.; Luo, A.-P.; Xing, X.-B.; Cui, H.; Luo, Z.-C.; Xu, W.-C. Coexistence of Rectangular and Gaussian-Shape Noise-Like Pulses in a Figure-Eight Fiber Laser. *Opt. Express* **2018**, *26*, 17804–17813. [CrossRef] [PubMed]
27. Guo, B.; Yao, Y.; Yang, Y.-F.; Yuan, Y.-J.; Jin, L.; Yan, B.; Zhang, J.-Y. Dual-Wavelength Rectangular Pulse Erbium-Doped Fiber Laser Based on Topological Insulator Saturable Absorber. *Photonics Res.* **2015**, *3*, 94–99. [CrossRef]
28. Guo, B.; Xiao, Q.-L.; Wang, S.-H.; Zhang, H. 2D Layered Materials: Synthesis, Nonlinear Optical Properties, and Device Applications. *Laser Photonics Rev.* **2019**, *13*, 1800327. [CrossRef]
29. Zhu, X.; Su, Z.; Wu, C.; Cong, H.; Ai, X.; Yang, H.; Qian, J. Exfoliation of MoS_2 Nanosheets Enabled by a Redox-Potential-Matched Chemical Lithiation Reaction. *Nano Lett.* **2022**, *22*, 2956–2963. [CrossRef] [PubMed]
30. Zhang, W.; Zheng, L.; Jiang, H.; Liu, N.; Yang, K.; Xian, T.; Zhan, L. Bright-Dark Pulse Pair in a Passively Mode-Locked Fiber Laser Based on Thulium-Doped Fiber. *IEEE Photonics Technol. Lett.* **2024**, *36*, 429–432. [CrossRef]
31. Wang, Z.; Luo, G.; Song, Y.; Deng, Z.; Liu, J.; Wen, Q.; Xu, C.; Zhang, C.; Cao, H. Transition from Pure-Quartic Solitons to Q-Switched Mode-Locking in an Ultrafast Fiber Laser. *Opt. Laser Technol.* **2026**, *203*, 115928. [CrossRef]
32. Zhang, T.; Meng, F.; Yan, Q.; Zhang, C.; Jia, Z.; Qin, W.; Qin, G.; Xu, H. Significant Enhancement of Multiple Resonant Sidebands in a Soliton Fiber Laser. *Photonics Res.* **2023**, *11*, 1847–1860. [CrossRef]
33. Liu, J.; Chen, Y.; Tang, P.; Xu, C.; Zhao, C.; Zhang, H.; Wen, S. Generation and Evolution of Mode-Locked Noise-Like Square-Wave Pulses in a Large-Anomalous-Dispersion Er-Doped Ring Fiber Laser. *Opt. Express* **2015**, *23*, 6418–6427. [CrossRef] [PubMed]
34. Santiago-Hernandez, H.; Pottiez, O.; Duran-Sanchez, M.; Alvarez-Tamayo, R.I.; Lauterio-Cruz, J.P.; Hernandez-Garcia, J.C.; Ibarra-Escamilla, B.; Kuzin, E.A. Dynamics of Noise-Like Pulsing at Sub-ns Scale in a Passively Mode-Locked Fiber Laser. *Opt. Express* **2015**, *23*, 18840–18849. [CrossRef] [PubMed]
35. Wang, Z.; Zhu, J.; Du, G.; Liu, J.; Song, Y. Noise-Like Rectangular Pulses with Asymmetric Spectral Stripes in a 1.7-μm Ultrafast Fiber Laser. *J. Light. Technol.* **2026**, *44*, 3218–3224. [CrossRef]
36. Goda, K.; Jalali, B. Dispersive Fourier Transformation for Fast Continuous Single-Shot Measurements. *Nat. Photonics* **2013**, *7*, 102–112. [CrossRef]
37. Li, Y.; Huang, D.; Shi, Y.; Wang, C.; Li, F. Statistical Dynamics of Noise-like Rectangle Pulse Fiber Laser. *Adv. Photon. Nexus* **2023**, *2*, 036005. [CrossRef]
38. Zhao, K.; Wang, P.; Ding, Y.; Yao, S.; Gui, L.; Xiao, X.; Yang, C. High-Energy Dissipative Soliton Resonance and Rectangular Noise-Like Pulse in a Figure-9 Tm Fiber Laser. *Appl. Phys. Express* **2019**, *12*, 012002. [CrossRef]

39. Wu, T.; Dou, Z.; Zhang, B.; Hou, J. Noise-Like Rectangular Pulses in a Mode-Locked Double-Clad Er:Yb Laser with a Record Pulse Energy. *Chin. Phys. B* **2020**, *29*, 014202. [CrossRef]
40. Schreiber, T.; Ortaç, B.; Limpert, J.; Tünnermann, A. On the Study of Pulse Evolution in Ultra-Short Pulse Mode-Locked Fiber Lasers by Numerical Simulations. *Opt. Express* **2007**, *15*, 8252–8262. [CrossRef] [PubMed]
41. Akhmediev, N.; Soto-Crespo, J.M.; Town, G. Pulsating Solitons, Chaotic Solitons, Period Doubling, and Pulse Coexistence in Mode-Locked Lasers: Complex Ginzburg-Landau Equation Approach. *Phys. Rev. E* **2001**, *63*, 056602. [CrossRef] [PubMed]
42. Chen, C.-J.; Wai, P.K.A.; Menyuk, C.R. Stability of Passively Mode-Locked Fiber Lasers with Fast Saturable Absorption. *Opt. Lett.* **1994**, *19*, 198–200. [CrossRef] [PubMed]
43. Jeon, J.; Lee, J.; Lee, J.H. Numerical Study on the Minimum Modulation Depth of a Saturable Absorber for Stable Fiber Laser Mode Locking. *J. Opt. Soc. Am. B* **2015**, *32*, 31–37. [CrossRef]
44. Lee, J.; Kwon, S.; Zhao, L.; Lee, J.H. Investigation into the Impact of the Recovery Time of a Saturable Absorber for Stable Dissipative Soliton Generation in Yb-Doped Fiber Lasers. *Opt. Express* **2021**, *29*, 21978–21991. [CrossRef] [PubMed]
45. Li, F.; Wai, P.K.A.; Kutz, J.N. Geometrical Description of the Onset of Multi-Pulsing in Mode-Locked Laser Cavities. *J. Opt. Soc. Am. B* **2010**, *27*, 2068–2077. [CrossRef]

Disclaimer/Publisher's Note: The statements, opinions and data contained in all publications are solely those of the individual author(s) and contributor(s) and not of MDPI and/or the editor(s). MDPI and/or the editor(s) disclaim responsibility for any injury to people or property resulting from any ideas, methods, instructions or products referred to in the content.